crystals

MDPI

Article

Tumor Microenvironment Activated Vanadium−Doped Carbon Dots for Fluorescence Imaging and Chemodynamic Therapy

Renhao Nie [2,3], Qingyan Jia [2,3,*] and Yunqi Li [1,*]

[1] Department of Gastroenterology, The First Medical Center, Chinese PLA General Hospital, Beijing 100853, China; iamrhnie@mail.nwpu.edu.cn
[2] Frontiers Science Center for Flexible Electronics (FSCFE), Shaanxi Institute of Flexible Electronics (SIFE) & Shaanxi Institute of Biomedical Materials and Engineering (SIBME), Northwestern Polytechnical University (NPU), 127 West Youyi Road, Xi'an 710072, China
[3] Frontiers Science Center for Flexible Electronics (FSCFE), Key Laboratory of Flexible Electronics of Zhejiang Province, Ningbo Institute of Northwestern Polytechnical University, 218 Qingyi Road, Ningbo 315103, China
* Correspondence: iamqyjia@nwpu.edu.cn (Q.J.); yunqi206@126.com (Y.L.)

Abstract: The multifunctional platform response to the tumor microenvironment (TME) is critical for the high-precision diagnosis and treatment of cancer with low systemic toxicity. In this regard, vanadium-doped carbon dots (V−CDs) have been developed for TME-activated fluorescence imaging and chemodynamic therapy (CDT). Due to the Forster resonance energy transfer caused by the doped vanadium, the obtained V−CDs displayed quenched fluorescence. Once entering the tumor, the fluorescence imaging ability of the V−CDs are stimulated by the reaction between vanadium and overexpressed H_2O_2 in a weak acid TME. Meanwhile, the hydroxyl radicals generated by the catalytic reaction of V−CDs could induce oxidative damage in tumor cells for CDT, while showing less cytotoxicity and side effects in normal cells. Therefore, the well-designed V−CDs could be used for TME-activated fluorescence imaging and CDT while maintaining an "inactive" status in normal tissues to ensure low biological toxicity, satisfying the clinical requirements for accurate diagnosis and efficient treatment with low side effects for tumors. Our research provides an effective strategy for designing and preparing multifunctional nanotheranostic drugs responsive to TME for accurate tumor imaging and treatment.

Keywords: carbon dot; fluorescence imaging; chemodynamic therapy; antitumor; tumor microenvironment

check for updates

Citation: Nie, R.; Jia, Q.; Li, Y. Tumor Microenvironment Activated Vanadium−Doped Carbon Dots for Fluorescence Imaging and Chemodynamic Therapy. *Crystals* **2023**, *13*, 652. https://doi.org/10.3390/cryst13040652

Academic Editor: Rajratan Basu

Received: 21 February 2023
Revised: 24 March 2023
Accepted: 4 April 2023
Published: 10 April 2023

Copyright: © 2023 by the authors. Licensee MDPI, Basel, Switzerland. This article is an open access article distributed under the terms and conditions of the Creative Commons Attribution (CC BY) license (https://creativecommons.org/licenses/by/4.0/).

1. Introduction

Due to the high incidence and mortality rates, cancer has become the number one killer threatening human health worldwide [1,2]. Common cancer treatments include surgery, chemotherapy, and radiotherapy, but these may result in adverse reactions, drug resistance, and long-term complications. The tumor microenvironment (TME) is the environment in which tumors occur, develop, and live, and its composition is complex, usually composed of cancer cells and a variety of stromal cells, cytokines, chemokines, etc. [3,4]. The characteristics of TME, such as abnormal vascular, high H_2O_2, acidic pH, and hypoxia, provide an internal environment for the origin and residence of cancer cells, and play a major role in tumor progression, invasive metastasis, and drug resistance [5,6]. Inversely, these TME characteristics also provide an effective target for tumor diagnosis and therapy and are highly valued when exploring new anti-cancer strategies [7–9]. Recently, smart nanomaterials responsive to TME have been proposed to achieve an accurate diagnosis and treatment of cancer, showing obvious advantages in improving treatment efficiency and reducing side effects [10–12]. Although extensive research has been done on the TME-triggered nanoplatform, there is still a strong desire to develop a simpler method to fabricate such nanoplatforms with satisfactory anti-tumor outcomes.

Fluorescence imaging has several advantages, including a low cost and low radiation risk, high sensitivity and resolution, and real-time imaging capture, making it suitable for tumor diagnosis [13,14]. Traditionally, fluorescent probes are used for imaging in their normally open state, which produces strong background signals and significantly reduces signal-to-noise ratios. In order to overcome these shortcomings, switched or activated fluorescence probes have been developed. For example, after interacting with the specific target, such as low pH values or high levels of GSH and H_2O_2 in the TME, the fluorescence probes could change from a quenched state to a non-quenched state [15,16]. For example, the content of H^+ and ATP in the tumor microenvironment is significantly higher than that in normal tissues. Professor Zhang's research team constructed pH- and ATP-responsive fluorescence probes based on the Forster resonance energy transfer using silicon rhodamine as a donor and CS dyes as receptors, which are suitable for imaging in living organisms and guiding tumor resection during surgery [17].

Carbon dots (CDs) have attracted widespread attention in the biomedical field, especially in tumor imaging and treatment, due to their extensive sources, rich functions, and safety/biocompatibility [18,19]. Because of their excellent and tunable multicolor emission, CDs have been widely used in fluorescence imaging to guide the treatment of tumors [20,21]. However, the non-specific distribution of CDs in normal organs, such as the liver and the kidneys, leads to the poor effect of tumor imaging with a low signal-to-background ratio. In addition, the common CDs used as photosensitizers or photothermal agents in tumor treatment also cause damage in normal tissues [22,23]. Developing CDs as fluorescence-imaging probes that respond to the TME and simultaneously activate their intrinsic therapeutic ability can provide a potential application for the accurate diagnosis and treatment of cancer [24].

Chemodynamic therapy (CDT) kills cancer cells by producing cytotoxic ·OH through the reaction of metal ions such as iron and copper and endogenous, overexpressed H_2O_2 in weak-acid TME, which has a high specificity in killing tumors and avoiding damage to normal tissues [25,26]. Doping metal in CDs can endow them with the unique characteristics of metal ions [27,28]. Vanadium (V) metallodrugs have recently been reported to inhibit tumor proliferation and metastasis. In particular, V ions can react with H_2O_2 in a Fenton-like manner to produce ·OH, in order to be used for tumor-specific CDT [29]. In addition, the therapeutic effect of CDT is easily affected by catalysts (e.g., the optimal pH range of iron-based derivatives is 3–4) and the over-expression of the antioxidant glutathione (GSH) in TME, which seriously hinders its further clinical transformation and application [30]. However, the multivalent states of V and its high-optimal catalytic pH range allow it to play a significant role in Fenton-like reactions and TME regulation [31,32]. Herein, we synthesized the V−doped CDs (V−CDs) with citric acid, urea, thioacetamide (TAA), and NH_4VO_3 using a facile hydrothermal treatment. The prepared V−CDs showed quenched fluorescence at 500–650 nm. However, after the reaction of the doped V with H_2O_2, the fluorescence of V−CDs can be restored for the fluorescence imaging of the tumor, and the ·OH can be produced for CDT at the same time. Therefore, in response to the overexpression of H_2O_2 in TME, the prepared V−CDs can achieve activated-specific fluorescence imaging and CDT, thus implementing the requirement for accurate diagnosis and treatment of tumors.

2. Materials and Methods

2.1. Materials and Apparatus

Citric acid, urea, TAA, H_2O_2, and NH_4VO_3 were obtained from Adamas. Dulbecco's modified Eagle's medium (DMEM) was purchased from Baoshun Biotechnology Co., Ltd. (Xi'an, China). Fetal bovine serum (FBS) was purchased from Sigma–Aldrich Trading Co., Ltd. (Shanghai, China). Trypsin was purchased from Life Technologies Corporation. Penicillin–Streptomycin Solution was provided by Regen Biotechnology Co., Ltd. (Beijing, China). Living/dead cell double staining kit was purchased from Vandersen Laboratory Equipment Co., Ltd. (Xi'an, China). Cell viability test dye, Alamar Blue, was purchased from Thermo Fisher Scientific.

Phosphate buffer saline (PBS) was purchased from saiguo Biotech Co., Ltd. (Guangzhou, China). H_2O_2 was obtained from Sinopharm Chemical Reagents Co., Ltd. (Xi'an, China). HeLa cells were provided by Servicebio Biotechnology Co., Ltd. (Wuhan, China). All chemicals used were analytical reagent grade or higher, and no further purification was required. Deionized (DI) water with a resistivity of 18 MΩcm was prepared using a Millipore Milli-Q system.

Transmission electron microscopy (TEM) was performed on FEI Talos F200X. The UV-vis and fluorescence spectra were acquired on a UV-3010 spectrophotometer (Hitachi) and an F-4500 fluorescence spectrophotometer (Hitachi). Fourier transform infrared spectra (FTIR) was recorded on a Bruker Tensor II FTIR spectrometer (Bremen). The X-ray photoelectron spectra (XPS) was acquired on an X-ray photoelectron spectrometer (Kratos). The spectra were processed with Case XPS v.2.3.12 using a peak fitting routine with symmetrical Gaussian–Lorentzian functions. The fluorescence images of HeLa cells were acquired on a Nikon confocal laser scanning microscope (CLSM).

2.2. Preparation of V−CDs

The V−CDs were prepared using one-pot hydrothermal carbonization. Firstly, 100 mg citric acid, 200 mg urea, 64.4 mg TAA, and 10 mg NH_4VO_3 were dissolved in 40 mL of ultra-pure water, and then placed in a stainless-steel autoclave with a PTFE liner (50 mL). After heating at 160 °C for 12 h, the vessel was cooled naturally to obtain a light purple solution, indicating the successful preparation of water-soluble V−CDs. Subsequently, large particles and precipitates in the solution were removed through centrifugation (10,000 rpm, 10 min, 25 °C) and filtering (Millipore, 0.22 μm). The V−CDs were further purified using a dialysis membrane (MWCO 1000 Da) for 24 h in ultra-pure water. Finally, the resulting aqueous solution was collected and freeze-dried to obtain the V−CDs in powder form, and then stored in a dry, ambient condition.

2.3. H_2O_2-Activated Fluorescence of V−CDs

50 μL V−CDs solution (2 mg/mL) was added to 2 mL H_2O_2 (1 mM) at pH 5, and then UV-vis and fluorescence spectrophotometers were used to measure the absorption (300–800 nm) and fluorescence (λ_{ex} = 480 nm) changes.

2.4. Detection of OH Generation

In order to evaluate the Fenton-like catalytic performance of V−CDs, 3,3′,5,5′-tetramethylbenzidine hydrochloride (TMB) was selected as the detection reagent, and the qualitative and quantitative tests were carried out by UV-visible spectrophotometry [33,34]. TMB reacts with strongly oxidizing ·OH and generates blue TMB+ (ox−TMB) with significant absorption at 652 nm. Its absorbance at 652 nm can be measured quantitatively using the UV−vis absorption spectrometer.

In order to determine the optimal pH for the peroxidase catalytic reaction of V−CDs, acetate buffer solutions with pH levels from 3 to 7 were prepared. V−CDs were added into the mixed solution of H_2O_2 (1 mM) and TMB (20 μg/mL) with pH levels of 3, 4, 5, 6, and 7, respectively, and the absorbance changes of the mixed solution within 5 min at 665 nm were measured using the multi-function microplate detector in time-scanning mode. The time-dependent changes in absorbance were statistically analyzed to obtain the optimal pH of V−CDs' catalytic reaction.

In order to investigate the effect of V−CDs concentration on catalytic reactions, V−CDs of different concentrations were added to a mixed solution of H_2O_2 and TMB, then the absorbance curve of different test groups at 550–800 nm were measured using an ultraviolet spectrophotometer.

In order to obtain the reaction and kinetic parameters of the V−CDs catalytic reactions, the concentration of the substrate TMB was changed, and the quantitative relationship between the catalytic reaction rate and the substrate concentration was explored. Buffer solutions, CDs, and TMB of different concentrations were added in the 96-well plate, and finally, H_2O_2 was added to initiate the reaction. After the reaction, the absorbance changes

of the solution at 665 nm were detected within 5 min using a multi-function microplate detector in a time-scanning mode.

2.5. In Vitro Fluorescence Imaging of V−CDs

In the cell culture flask, the HeLa cells were resuscitated using a DMEM high-sugar medium (5 mL, containing 10% fetal bovine serum and 1% penicillin mixture). HeLa cells were cultured in a constant temperature incubator with parameters set at 37 °C and 5% CO_2. When HeLa cells were in good condition and full grown, 1 mL of trypsin was added to digest the cells, transforming them from an adherent state to a floating form for cell passage. The cells with high cell viability after passage were used for subsequent cell experiments.

HeLa cells were seeded into 35 mm confocal dishes at a concentration of 1×10^5 cells per dish and incubated at 37 °C under 5% CO_2 for 12 h. After washing with PBS, the cells were incubated with a DMEM medium containing 25 μg/mL of V−CDs for 4 h at 37 °C, and then added to 100 μM H_2O_2 with a further incubation of 3 h. Next, the fluorescence of V−CDs in cells was observed by a laser confocal microscope (λ_{ex} = 488 nm). The V−CDs-treated cells without H_2O_2 addition were used as control. The NIH3T3 cells were resuscitated using the same method as described above, with newborn bovine serum, and incubated in a 96-well plate in a cell incubator for 12 h. The cells were incubated with different concentrations of V−CDs for 12 h, and then added to 100 μM of Alamar Blue for an incubation period of 6 h. The fluorescence intensity of 590 nm under the excitation of 530 nm wavelength was measured by a multifunctional microplate detector.

2.6. In Vitro Cytotoxicity and CDT of V−CDs

HeLa cells were seeded in 96-well plates (1×10^4 cells per well) and incubated at 37 °C under 5% CO_2 for 12 h. The cells were incubated with different concentrations of V−CDs for 12 h, and then added to 100 μM H_2O_2 with a further incubation period of 12 h. After adding Alamar Blue for an incubation period of 6 h, the fluorescence intensity of 590 nm under the excitation of 530 nm wavelength was measured by a multifunctional microplate detector. Cell survival rate was calculated as follows: (Cell Viability = ($OD_{treated}$ − OD_{blank})/($OD_{control}$ − OD_{blank}) × 100%. In this equation, $OD_{treated}$ represents the fluorescence intensity of the CDs treat group, and $OD_{control}$ and OD_{blank} represent the fluorescence intensity of the control group and the blank group, respectively. The V−CDs-treated cells without H_2O_2 addition were used as control.

The cytotoxicity of the V−CDs was further evaluated by Calcein AM/propidium iodide (PI) staining. Before use, the working solution was diluted 10 times with serum-free DMEM high-sugar medium as a dye solvent, then 1 μL AM and 2 μL PI dye was added into 2mL diluent and shaken well for standby. HeLa cells were then seeded in confocal dishes (1×10^5 cells per dish) and incubated for 12 h. The cells were incubated with different concentrations of V−CDs for 12 h, and then added to 100 μM H_2O_2 with a further incubation period of 12 h. After that, the fresh DMEM medium containing 5 μM Calcein AM and 5 μM PI was added for an incubation period of 0.5 h. After dyeing, the cells were washed with PBS three times to. The bright green/red fluorescence was captured by a laser confocal microscope (λ_{ex} = 488/543 nm). The V−CDs-treated cells without H_2O_2 addition were used as control.

3. Results

3.1. Characterization of V−CDs

The V−CDs were successfully prepared by the hydrothermal treatment of citric acid, urea, TAA, and NH_4VO_3 at 160 °C for 12 h. The prepared V−CDs were determined by TEM. As shown in Figure 1a, V−CDs were observed to be well-dispersed quasi-sphere nanoparticles with 3–5 nm. The high-resolution TEM (HR−TEM) image exhibits that the lattice spacing of V−CDs was 0.21 nm, demonstrating their graphite-like structure (Figure 1b) [35]. The XRD pattern of V−CDs shows a peak at 2θ = 30° (Figure 1c), suggesting that the dominant carbon species is sp^2-hybridized [36].

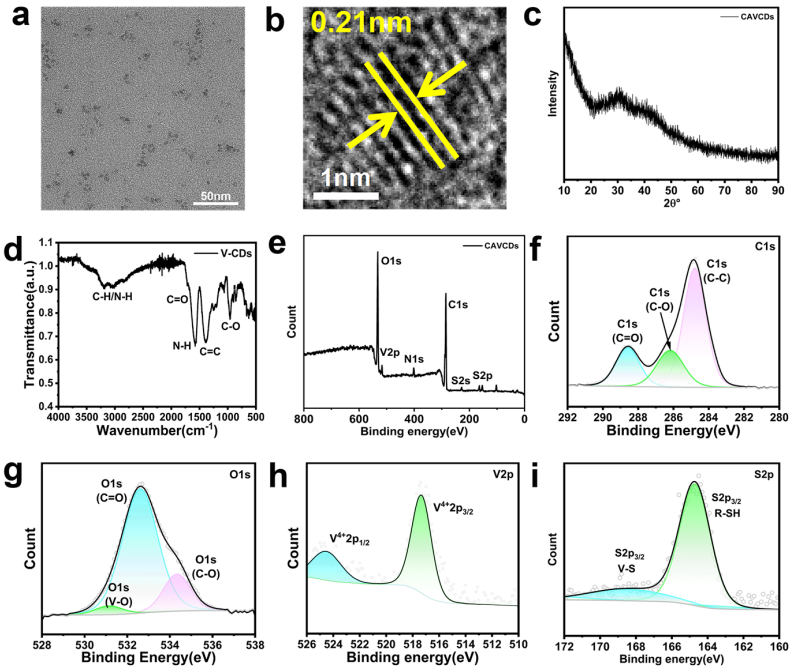


Figure 1. (**a**) TEM image of V−CDs. (**b**) HRTEM image of V−CDs. (**c**) XRD pattern of V−CDs. (**d**) FTIR spectra of V−CDs. (**e**) XPS survey spectra of V−CDs. The high resolution XPS spectrum of V−CDs: (**f**) C1s, (**g**) O1s, (**h**) V2p, and (**i**) S2p, respectively.

FTIR was carried out to investigate the chemical compositions of V−CDs. In the FTIR spectra, V−CDs exhibited obvious peaks at about 950, 1381, 1568, 2992, and 3183 cm^{-1}, suggesting the presence of carboxyl (−COOH), amino (−NH_2), and hydroxyl (−OH) groups (Figure 1d), which ensure the excellent water solubility of V−CDs [37]. Additionally, XPS was performed to further confirm the chemical compositions of V−CDs (Figure 1e). The survey spectrum of V−CDs exhibited five characteristic peaks of C1s (284.8 eV), N1s (399.8 eV), O1s (531.7 eV), V2p (516.4 eV), and S2p (164.7 eV). The high-resolution C1s spectrum (Figure 1f) revealed three different C types of C=C, C=O, and C-O. Moreover, the O1s spectrum showed three peaks of C=O, C−O, and V−O (Figure 1g). The V2p spectrum (Figure 1h) showed two peaks at 517.4, and 524.5 eV, which were assigned to V^{4+}2p3/2 and V^{4+}2p1/2, respectively. The S2p spectrum showed two peaks of R-SH and V-S (Figure 1i) [38]. All of the above results proved the successful preparation of V−CDs, and the doped coordinated with S and O in the form of a tetravalent state.

3.2. Fluorescence and ·OH Generation

In order to study the optical properties of V−CDs, we prepared CACDs as a control by a hydrothermal treatment of citric acid, urea, and TAA without adding NH_4VO_3. As shown in Figure 2a, the UV-vis spectrum of CACDs exhibited an absorption peak at 340 nm, which is ascribed to a π−π* transition of the aromatic C=C bond. In addition to the absorption peak of the π−π* transition of the aromatic C=C bond at 332 nm, V−CDs also showed a new absorption peak at 560 nm due to the doping of V. However, the absorption peak of V−CDs at 560 nm disappeared with H_2O_2 addition. Additionally, CACDs could emit fluorescence in the range of 500–650 nm, while the fluorescence of V−CDs was quenched due to V doping (Figure 2b). Amazingly, in the presence of 1 mM H_2O_2, the fluorescence of V−CDs recovered at a pH of 5, which may be attributed to the V oxidation reacting with H_2O_2 and being released from the CACDs. The fluorescence recovery mechanism is inferred from the existing literature reports as follows: on the one hand, the metal V binds to CDs through solitary electron pairs on oxygen atoms, and this ligand structure tends to confine carriers within the core of V−CDs. When metal V is oxidized and released from V−CDs and becomes ionic, it floats in the solution, thus liberating groups such as −COOH/−OH on the surface of V−CDs. Changes

in charged-surface groups cause the separation of electron hole pairs, making photo-induced charge transfer possible. On the other hand, the doping of V metal changes the conduction band and valence band positions of CDs, and increases the energy band gap value, making transitions difficult. When H_2O_2 oxidizes the metal V into an ionic state and releases it from V−CDs, the excitation energy is lower than the difference in the energy band gap transitions, restoring the photoluminescence behavior of CDs [39,40]. As reported, V^{4+} can catalyze H_2O_2 to produce ·OH according to Formula of $V^{4+} + H_2O_2 + H^+ \rightarrow V^{5+} + H_2O + OH$ [41]. To evaluate the ROS generation through a Fenton-like reaction induced by V−CDs, TMB was selected as the capture probe of ·OH, which shows an obvious absorption peak at 652 nm and makes the solution blue (Figure 3a) [42]. Firstly, pH-dependent catalytic performances of V−CDs were studied. As shown in Figure 3b, pH 5.0 is the most favorable for enzyme-like activity. Thereby, the optimal catalytic condition (pH 5.0) was selected to study the catalytic properties of V−CDs. Subsequently, the effect of the concentration of V−CDs on the catalytic performance was studied. As displayed in Figure 3c, the mixed solution containing TMB and H_2O_2 treated with V−CDs at pH 5 had an obvious absorption peak at 652 nm, and gradually increased with the increase of V−CDs concentration. However, in the absence of H_2O_2, the absorption of the mixture solution hardly changed. All these results confirmed that V−CDs can effectively catalyze H_2O_2 to produce ·OH. Additionally, the maximum initial velocity (V_{max}) and the Michaelis–Menten constant (K_m) were obtained from the Lineweaver–Burk plot to analyze the kinetic parameters of V−CD (Figure 3d). The V_{max} and K_m values of V−CDs were determined to be 143.2×10^{-8} M S^{-1} and $(2.019 \times 10^{-1}) \times 10^{-3}$ M, respectively, with TMB as a substrate, which are similar to the kinetic parameters of reported CDs [42]. In summary, the weak acid and high level of H_2O_2 simulating the TME can promote the release of V^{4+} from V−CDs, leading to the activation of fluorescence and the "switch on" of CDT.

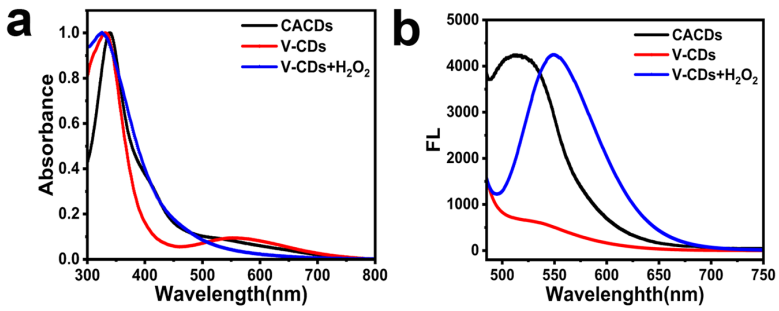


Figure 2. (**a**) UV−vis spectrum of CACDs, V−CDs, and H_2O_2 treated V−CDs. (**b**) Fluorescence spectra of CACDs, V−CDs, and H_2O_2 treated V−CDs at excitation wavelengths of 480 nm.

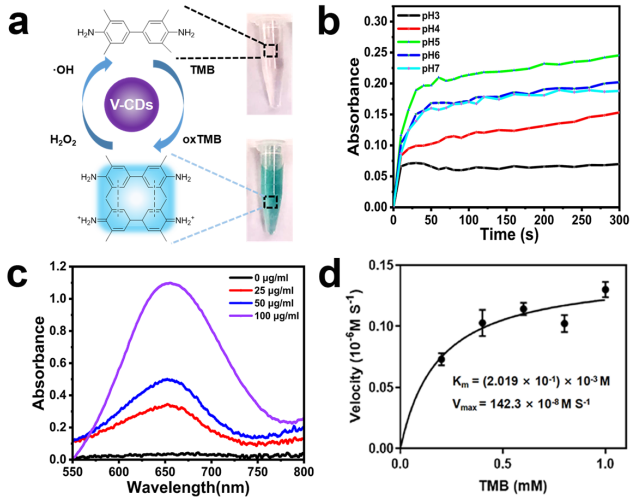


Figure 3. (**a**) Schematic illustration of TMB used to detect OH produced by V−CDs catalytic H_2O_2. (**b**) Catalytic activity of V−CDs for TMB oxidation at various pH values. (**c**) Absorption spectra of

TMB in the presence of H_2O_2 at different concentrations of V−CDs. (**d**) Steady state kinetic assay of V−CDs catalytic activity.

3.3. In Vitro Fluorescence Imaging

As proved in the solution, V doping could cause fluorescence quenching of V−CDs due to heavy atom effect. In the presence of H_2O_2, V^{4+} in the V−CDs can be oxidized to V^{5+}, which releases from the V−CDs to restore the fluorescence of V−CDs. Subsequently, we evaluated the fluorescence imaging of HeLa cells treated by V−CDs under the stimulation of excessive H_2O_2 using CLSM. As shown in Figure 4, when there is no H_2O_2, no fluorescence was observed in the V−CDs-treated HeLa cells. With the addition of H_2O_2, the fluorescence emitted by V−CDs could be observed in HeLa cells. Under the excitation of a 488 nm laser, green emissions within the range of 510 to 540 nm could be collected and uniformly distributed in HeLa cells, indicating that V−CDs are effectively absorbed through endocytosis. All these results show that the prepared V−CDs can be used as a TME stimuli-responsive nanoprobe for in vitro biological multicolor fluorescence imaging.

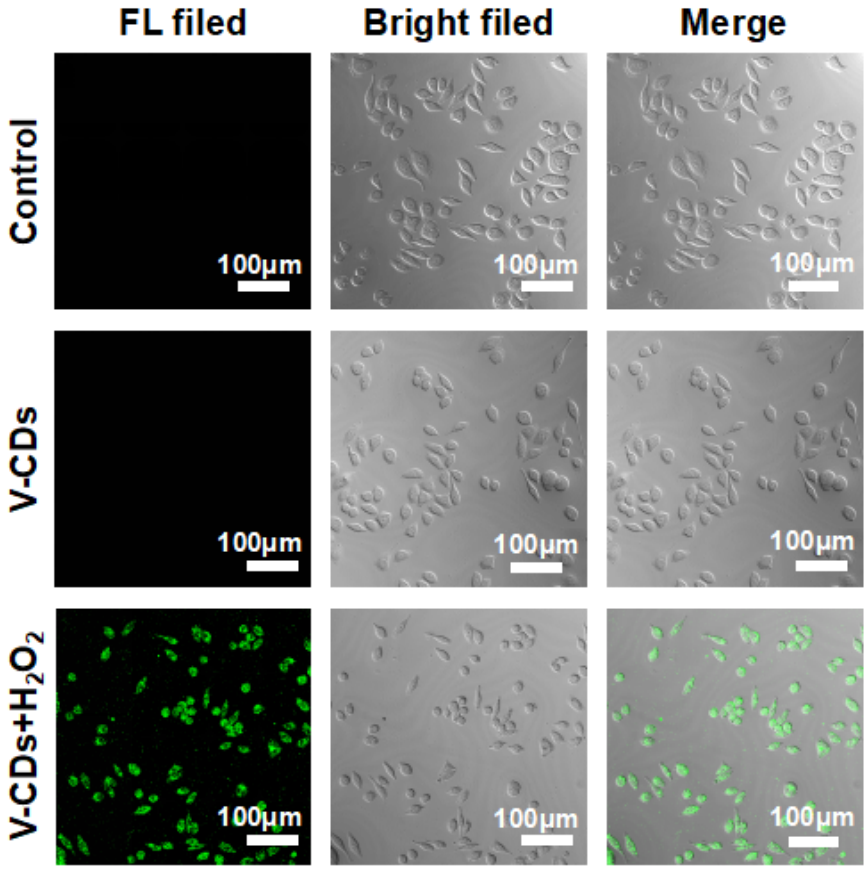


Figure 4. Confocal laser scanning microscope fluorescence images of V−CDs−treated HeLa cells with or without H_2O_2. The images of bright field, and the overlay for the corresponding samples were recorded. Scale bar represents 100 μm.

3.4. In Vitro Cytotoxicity and CDT of V−CDs

Cell proliferation is an important life feature of organisms, and is the basis for the growth, development, reproduction, and inheritance of organisms. New cells are produced through cell division in the organism to supplement the aging or dead cells in the body. Therefore, the proliferation activity of cells is also one of the criteria used to measure the strength of cell function. The proliferation activity of damaged cells is weak, while the proliferation activity of tumor cells is often very active. Therefore, in order to measure the effect of V−CDs and CDT on HeLa cells, the cell activity test was carried out.

NIH3T3 cells were selected to study the cytotoxicity of V−CDs. As shown in Figure 5a, when the concentration of V−CDs was 100 μg/mL, the cell viability of NIH3T3 cells was close to 90%. The experimental results indicated that V−CDs have low toxicity and good biocompatibility. The produced ·OH could lead to cell oxidative damage and cause them to die. Next, we determined the lethal activity of V−CDs on HeLa cells using Alamar Blue staining. Figure 5b shows that HeLa cells still maintained a high survival rate after co-incubation with V−CDs for 24 h. When the concentration of V−CDs was 100 μg mL^{-1}, the cell survival rate was still higher than 90%. With the addition of 100 μM H_2O_2, the cell survival rate decreased with the increase of V−CDs concentration, and the cell death rate reached 60% at the concentration of 100 μg mL^{-1}. Therefore, within a certain concentration range (≈100 μg/mL), V−CDs have high biological safety and can respond to the high level of H_2O_2 in TME to kill tumor cells effectively and specifically.

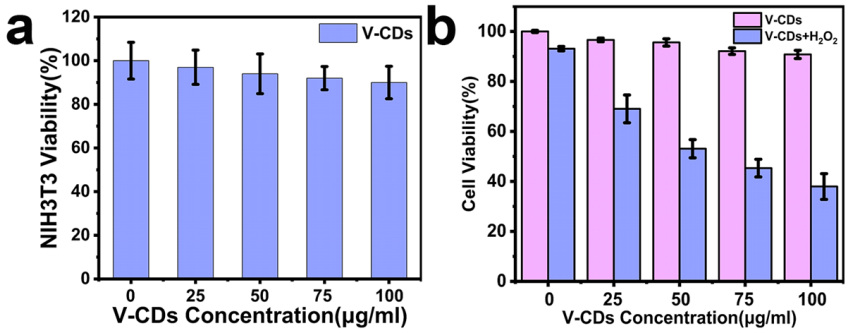


Figure 5. (**a**) The viability NIH3T3 cells incubated with various concentrations of V−CDs. (**b**) The viability HeLa cells incubated with various concentrations of V−CDs in the presence of H_2O_2.

The living cell/dead cell double staining probe includes the living cell fluorescence probe calcein AM and the dead cell fluorescence probe PI. Calcein AM is a hydrophobic compound that can easily penetrate intact living cells. After entering the cells, it is hydrolyzed by esterase to produce strong fluorescence. At the same time, it can be completely stored in the cytoplasm of cells. The esterase activity is proportional to the number of living cells. For living cells with intact membranes, the DNA dye PI is polar and cannot penetrate the cell membrane. It can only bind to the DNA of dead cells. Thus, AM is used to mark living cells, which dyes living cells green, while PI is used to mark dead cells, which dyes dead cells red.

The calcein AM/PI staining experiment was carried out to further prove the specific CDT efficacy of V−CDs. As shown in Figure 6a, in the V−CDs-treated groups, only green (live) and no red (dead) fluorescence was observed, agreeing well with the low cytotoxicity of CACDs. Since only a few dead cells lost their adherent state, resulting in being washed out during the process of staining, the red fluorescence in the picture is not obvious. With the addition of H_2O_2, the green fluorescence gradually weakened, while the red fluorescence improved with the increase of the concentration of V−CDs (Figure 6b), verifying the excellent H_2O_2-activated CDT efficacy of V−CDs.

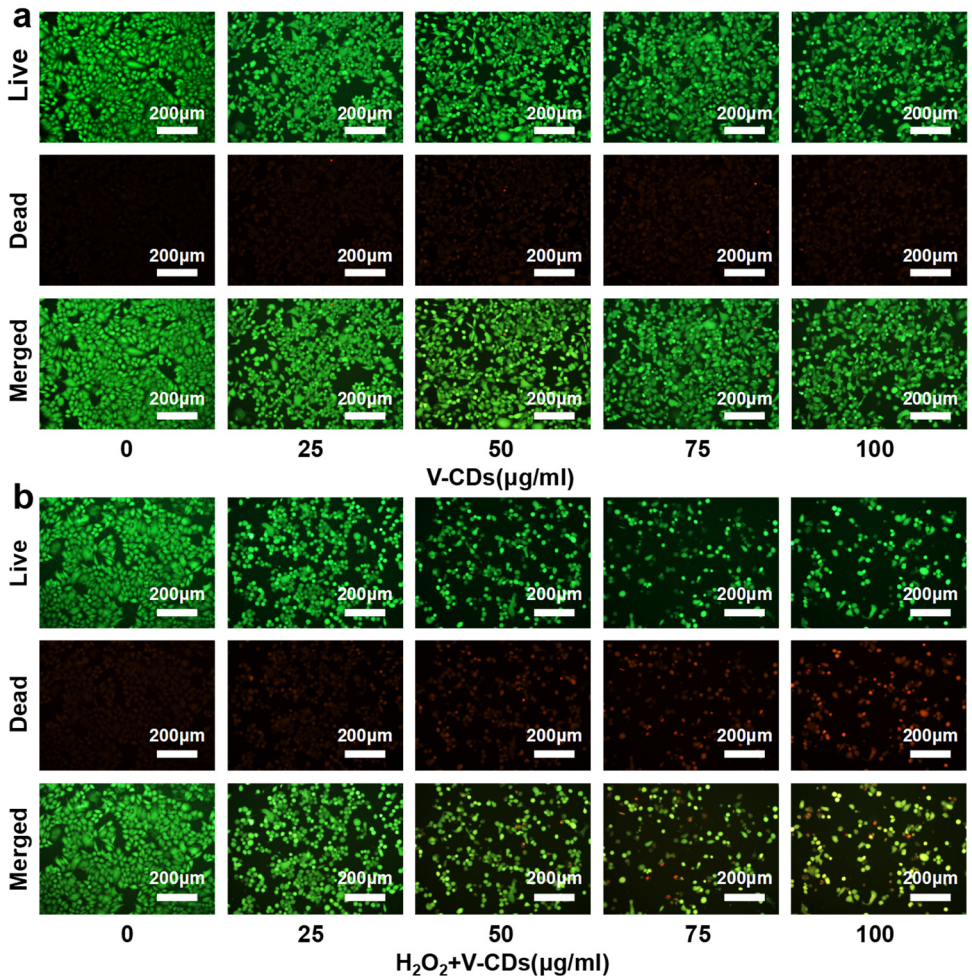


Figure 6. Live/dead staining of HeLa cells (**a**) HeLa cell treated with different concentrations V−CDs. Control was cells not treated with V−CDs. and (**b**) HeLa cell treated with different concentrations V−CDs in the presence of H_2O_2. Control was cells not treated with V−CDs. Scale bar represents 200 μm.

3.5. Comparison of the Performance of Fluorescent and Peroxidase-like CDs

We further compared the as-prepared diagnosis and treatment integration CDs with those currently reported (Table 1). The existing multifunctional-integrated nanocomposites for fluorescence diagnosis and chemokinetic therapy are composed of multiple reagents, which have difficulty ensuring stability and pose a risk of disassembly in organisms. In our work, the as-prepared green fluorescent V−CDs were prepared using a one-pot method with the common citric acid urea hydrothermal system, which can be directly used without modification after successful preparation. The versatility of V−CDs stems from their own structure, and due to its high stability, there is no potential disassembly risk. Better luminescence behaviour and higher catalytic efficiency was demonstrated, compared to the reported systems. Overall, the performance of the prepared CDs−based assay is comparable to or even better than those reported in the literature.

Table 1. Comparison with other types of CDs previously reported in terms of stability, cell imaging, and CDT.

Materials	Assembled or Decorated	Response Conditions	Emission Fluorescence	Km/mM	Vmax/10^{-8} Ms^{-1}	Ref
V−CDs	No	H_2O_2	Green	0.2019	142.3	This work
CDs@EDTA@Gd@Fe	Yes	pH	Red	Not tested		[43]

Table 1. *Cont.*

Materials	Assembled or Decorated	Response Conditions	Emission Fluorescence	Km/mM	Vmax/10^{-8} Ms^{-1}	Ref
Fe-decorated CDs	Yes	GSH	Blue	Not tested		[44]
g-CNQDs-PEG	Yes	pH	Green	Not tested		[45]
Fe-Ce6-RCDs	Yes	pH	Red	Not tested		[46]

4. Discussion

In this study, we have successfully fabricated an intelligent anti-cancer theranostic platform, referred to as V−CDs, using a simple and rapid one-pot hydrothermal method. Notably, the introduction of V in CDs not only provided luminescence in response to TME stimulation, but also offered effective CDT function by generating ·OH through a reaction with H_2O_2. As evidenced in in vitro experiments, the V−CDs could make HeLa cells present green fluorescence in response to H_2O_2, and also confirmed the effectiveness and high specificity of the CDT effect induced by V^{4+} through the Fenton-like reaction. The platform boasted impressive features of TME stimuli-responsive fluorescence imaging and synergistic CDT. In addition, V−CDs did not exhibit significant cytotoxicity on normal cells. Compared to the reported nanocomposites, they have high stability, good luminescent behavior, and high catalytic efficiency, without having potential disassembly risks. The well-designed V−CDs could effectively enhance therapeutic efficacy with minimized side effects by fully taking advantage of the TME, providing a novel strategy for the integrated diagnosis and treatment of cancer.

Author Contributions: Conceptualization, Y.L. and Q.J.; methodology, R.N.; resources, Y.L. and Q.J., and R.N.; data curation, Y.L. and Q.J.; writing—original draft preparation, R.N. and Q.J. All authors have read and agreed to the published version of the manuscript.

Funding: This work was supported by the National Natural Science Foundation of China (Grant Nos. 52273302 and 51902262).

Institutional Review Board Statement: Not applicable.

Informed Consent Statement: Not applicable.

Data Availability Statement: Not applicable.

Conflicts of Interest: The authors declare no conflict of interest.

References

1. Torre, L.A.; Bray, F.; Siegel, R.L. Global Cancer Statistics, 2012. *CA Cancer J. Clin.* **2015**, *65*, 87–108. [CrossRef] [PubMed]
2. Lambert, A.W.; Pattabiraman, D.R.; Weinberg, R.A. Emerging Biological Principles of Metastasis. *Cell* **2017**, *168*, 670–691. [CrossRef] [PubMed]
3. Anderson, N.M.; Simon, M.C. The tumor microenvironment. *Curr. Biol.* **2020**, *30*, R921–R925. [CrossRef] [PubMed]
4. Kiran, A.V.V.V.R.; Kumari, G.K.; Krishnamurthy, P.T.; Khaydarov, R.R. Tumor microenvironment and nanotherapeutics: Intruding the tumor fort. *Biomater. Sci.* **2021**, *9*, 7667. [CrossRef] [PubMed]
5. Arneth, B. Tumor Microenvironment. *Medicina* **2020**, *56*, 15. [CrossRef] [PubMed]
6. Paskeh, M.D.A.; Entezari, M.; Mirzaei, S.; Zabolian, A.; Saleki, H.; Naghdi, M.J.; Sabet, S.; Khoshbakht, M.A.; Hashemi, M.; Hushmandi, K.; et al. Emerging role of exosomes in cancer progression and tumor microenvironment remodeling. *J. Hematol. Oncol.* **2022**, *15*, 83. [CrossRef] [PubMed]
7. Xiao, Y.; Yu, D. Tumor microenvironment as a therapeutic target in cancer. *Pharmacol. Ther.* **2021**, *221*, 107753. [CrossRef]
8. Bai, Y.; Shu, T.; Su, L.; Zhang, X. Fluorescent Gold Nanoclusters for Biosensor and Bioimaging Application. *Crystals* **2020**, *10*, 357. [CrossRef]
9. Shim, M.K.; Yang, S.; Sun, I.-C.; Kim, K. Tumor-activated carrier-free prodrug nanoparticles for targeted cancer Immunotherapy: Preclinical evidence for safe and effective drug delivery. *Adv. Drug Deliv. Rev.* **2022**, *183*, 114177. [CrossRef]
10. Zhang, X.; An, L.; Tian, Q.; Lin, J.; Yang, S. Tumor microenvironment-activated NIR-II reagents for tumor imaging and therapy. *J. Mater. Chem. B* **2020**, *8*, 4738–4747. [CrossRef]
11. Thakkar, S.; Sharma, D.; Kalia, K.; Tekade, R.K. Tumor microenvironment targeted nanotherapeutics for cancer therapy and diagnosis: A review. *Acta Biomater.* **2020**, *101*, 43–68. [CrossRef]

12. Shen, G.; Hu, M.; Qi, J. Progress of Luminescent Carbon Dots in Biomedicine Engineering. *Nano Biomed. Eng.* **2016**, *8*, 190–202. [CrossRef]
13. Kim, H.; Kwak, G.; Kim, K.; Yoon, H.Y.; Kwon, I.C. Theranostic designs of biomaterials for precision medicine in cancer therapy. *Biomaterials* **2019**, *213*, 119207. [CrossRef]
14. David, A.M.; Michael, D.F.; Amy, S.C. Making Molecular Imaging a Clinical Tool for Precision Oncology. *JAMA Oncol.* **2017**, *3*, 695–701.
15. Lee, J.Y.; Choi, D.-Y.; Cho, M.Y.; Park, K.E.; Lee, S.-H.; Cho, S.H.; Hong, K.S.; Lim, Y.T. Targeted Theranostic Nanoparticles: Receptor-Mediated Entry into Cells, pH-Induced Signal Generation and Cytosolic Delivery. *Small* **2014**, *10*, 901–906. [CrossRef]
16. Ansari, G.A.C.; Tikhomirov, S.H.; Hong, R.A.; Falconer, P.M.; Loadman, J.H.; Gill, R.; Castaneda, F.K.; Hazard, L.; Tong, O.D.; Lenkov, D.W.; et al. Development of novel tumor-targeted theranostic nanoparticles activated by membrane-type matrix metalloproteinases for combined cancer magnetic resonance imaging and therapy. *Small* **2014**, *10*, 566–575. [CrossRef]
17. Liu, X.; Gong, X.; Yuan, J.; Fan, X.; Zhang, X.; Ren, T.; Yang, S.; Yang, R.; Yuan, L.; Zhang, X. Dual-Stimulus Responsive Near-Infrared Reversible Ratiometric Fluorescent and Photoacoustic Probe for In Vivo Tumor Imaging. *Anal. Chem.* **2021**, *93*, 5420–5429. [CrossRef]
18. Jia, Q.; Zhao, Z.; Liang, K.; Nan, F.; Li, Y.; Wang, J.; Ge, J.; Wang, P. Recent advances and prospects of carbon dots in cancer nanotheranostics. *Mater. Chem. Front.* **2020**, *4*, 449–471. [CrossRef]
19. Zhang, Y.; Jia, Q.; Nan, F.; Wang, J.; Liang, K.; Li, J.; Xue, X.; Ren, H.; Liu, W.; Ge, J.; et al. Carbon dots nanophotosensitizers with tunable reactive oxygen species generation for mitochondrion-targeted type I/II photodynamic therapy. *Biomaterials* **2023**, *293*, 121953. [CrossRef]
20. Shang, W.; Xia, X.; Lu, N.; Gao, P.; Peng, L.; Liu, Y.; Deng, H.; Jiang, J.; Li, Z.; Liu, J. Colourful fluorescence-based carbon dots for tumour imaging-guided nanosurgery. *Nanomedicine* **2022**, *45*, 102583. [CrossRef]
21. Ou, S.-F.; Zheng, Y.-Y.; Lee, S.-J.; Chen, S.-T.; Wu, C.-H.; Hsieh, C.-T.; Juang, R.-S.; Peng, P.-Z.; Hsueh, Y.-H. N-Doped Carbon Quantum Dots as Fluorescent Bioimaging Agents. *Crystals* **2021**, *11*, 789. [CrossRef]
22. Lagos, K.J.; Buzzá, H.H.; Bagnato, V.S.; Romero, M.P. Carbon-Based Materials in Photodynamic and Photothermal Therapies Applied to Tumor Destruction. *Int. J. Mol. Sci.* **2021**, *23*, 22. [CrossRef] [PubMed]
23. Liu, H.; Mo, L.; Chen, H.; Chen, C.; Wu, J.; Tang, Z.; Guo, Z.; Hu, C.; Liu, Z. Carbon Dots with Intrinsic Bioactivities for Photothermal Optical Coherence Tomography, Tumor-Specific Therapy and Postoperative Wound Management. *Adv. Healthc. Mater.* **2022**, *11*, 2101448. [CrossRef] [PubMed]
24. Sun, S.; Chen, Q.; Tang, Z.; Liu, C.; Li, Z.; Wu, A.; Lin, H. Tumor Microenvironment Stimuli-Responsive Fluorescence Imaging and Synergistic Cancer Therapy by Carbon-Dot-Cu(2+) Nanoassemblies. Angew. *Chem. Int. Ed.* **2020**, *59*, 21041–21048. [CrossRef]
25. Zhao, D.-H.; Li, C.-Q.; Hou, X.-L.; Xie, X.-T.; Zhang, B.; Wu, G.-Y.; Jin, F.; Zhao, Y.-D.; Liu, B. Tumor Microenvironment-Activated Theranostics Nanozymes for Fluorescence Imaging and Enhanced Chemo-Chemodynamic Therapy of Tumors. *ACS Appl. Mater. Interfaces* **2021**, *13*, 55780–55789. [CrossRef]
26. Tang, Z.; Liu, Y.; He, M.; Bu, W. Chemodynamic Therapy: Tumour Microenvironment-Mediated Fenton and Fenton-like Reactions. *Angew. Chem. Int. Ed.* **2019**, *58*, 946–956. [CrossRef]
27. Liang, K.; Ge, J.; Wang, P. Emerging metal doped carbon dots for promising theranostic applications. *Biomed. Mater.* **2023**, *18*, 012001. [CrossRef]
28. Li, X.; Fu, Y.; Zhao, S.; Xiao, J.; Lan, M.; Wang, B.; Zhang, K.; Song, X.; Zeng, L. Metal ions-doped carbon dots: Synthesis, properties, and applications. *Chem. Eng. J.* **2022**, *430*, 133101. [CrossRef]
29. Chen, T.; Huang, R.; Liang, J.; Zhou, B.; Guo, X.L.; Shen, X.-C.; Jiang, B.-P. Natural Polyphenol–Vanadium Oxide Nanozymes for Synergistic Chemodynamic/Photothermal Therapy. *Chemistry* **2020**, *26*, 15159–15169. [CrossRef]
30. Liu, X.; Yan, Z.; Zhang, Y.; Liu, Z.; Sun, Y.; Ren, J.; Qu, X. Two-Dimensional Metal–Organic Framework/Enzyme Hybrid Nanocatalyst as a Benign and Self-Activated Cascade Reagent for in Vivo Wound Healing. *ACS Nano* **2019**, *13*, 5222–5230. [CrossRef]
31. Selvaraj, S.; Krishnan, U.M. Vanadium–Flavonoid Complexes: A Promising Class of Molecules for Therapeutic Applications. *J. Med. Chem.* **2021**, *64*, 12435–12452. [CrossRef]
32. Feng, W.; Han, X.; Hu, H.; Chang, M.; Ding, L.; Xiang, H.; Chen, Y.; Li, Y. 2D vanadium carbide MXenzyme to alleviate ROS-mediated inflammatory and neurodegenerative diseases. *Nat. Commun.* **2021**, *12*, 2203. [CrossRef]
33. Zhang, X.; Yang, Q.; Lang, Y.; Jiang, X.; Wu, P. Rationale of 3,3′,5,5′-Tetramethylbenzidine as the Chromogenic Substrate in Colorimetric Analysis. *Anal. Chem.* **2020**, *92*, 12400–12406. [CrossRef]
34. Tang, Y.; Chen, Y.; Liu, Y.; Xia, Y.; Zhao, F.; Zeng, B. Detection of Gastric Cancer-Associated d-Amino Acids and Carcinoembryonic Antigen by Colorimetric and Immuno ECL Sensing Platform Based on the Catalysis of N/S-Doped Carbon Dots @ N-Rich Porous Carbon Nanoenzyme. *Anal. Chem.* **2022**, *94*, 17787–17794. [CrossRef]
35. Wang, Z.; Liu, L.; Bu, W.; Zheng, M.; Jin, N.; Zhang, K.; Xu, X.; Zhou, D.; Yang, B.; Sun, H. Carbon Dots Induce Epithelial-Mesenchymal Transition for Promoting Cutaneous Wound Healing via Activation of TGF-β/p38/Snail Pathway. *Adv. Funct. Mater.* **2020**, *30*, 2004886. [CrossRef]
36. Strauss, V.; Wang, H.; Delacroix, S.; Ledendecker, M.; Wessig, P. Carbon nanodots revised: The thermal citric acid/urea reaction. *Chem. Sci.* **2020**, *11*, 8256–8266. [CrossRef]

37. Yao, X.; Wang, Y.; Li, F.; Dalluge, J.J.; Orr, G.; Hernandez, R.; Cui, Q.; Haynes, C.L. Unconventional aliphatic fluorophores discovered as the luminescence origin in citric acid–urea carbon dots. *Nanoscale* **2022**, *14*, 9516–9525. [CrossRef]
38. Liang, S.; Liu, B.; Xiao, X.; Yuan, M.; Yang, L.; Ma, P.; Cheng, Z.; Lin, J. A Robust Narrow Bandgap Vanadium Tetrasulfide Sonosensitizer Optimized by Charge Separation Engineering for Enhanced Sonodynamic Cancer Therapy. *Adv. Mater.* **2021**, *33*, e2101467. [CrossRef]
39. Prashant, K.S.; Michael, L.F. Light emitting diodes based on carbon dots derived from food, beverage, and combustion wastes. *Phys. Chem. Chem. Phys.* **2015**, *17*, 27642.
40. Dhiman, B.; Prashant, K.S.; Michael, L.F. Quantum dots and carbon dots based fluorescent sensors for TB biomarkers detection. *Vacuum* **2017**, *146*, 606–613.
41. Yang, B.; Chen, Y.; Shi, J. Reactive Oxygen Species (ROS)-Based Nanomedicine. *Chem. Rev.* **2019**, *119*, 4881–4985. [CrossRef] [PubMed]
42. Wang, H.; Liu, C.; Liu, Z.; Ren, J.; Qu, X. Specific Oxygenated Groups Enriched Graphene Quantum Dots as Highly Efficient Enzyme Mimics. *Small* **2018**, *14*, e1703710. [CrossRef] [PubMed]
43. Wang, W.; Zhang, Q.; Zhang, M.; Liu, Y.; Shen, J.; Zhou, N.; Lu, X.; Zhao, C. Multifunctional red carbon dots: A theranostic platform for magnetic resonance imaging and fluorescence imaging-guided chemodynamic therapy. *Analyst* **2020**, *145*, 3592–3597. [CrossRef] [PubMed]
44. Li, J.; Hu, Z.-E.; We, Y.-J.; Liu, Y.-H.; Wang, N.; Yu, X.-Q. Multifunctional carbon quantum dots as a theranostic nanomedicine for fluorescence imaging-guided glutathione depletion to improve chemodynamic therapy. *J. Colloid Interface Sci.* **2022**, *606*, 1219–1228. [CrossRef]
45. Zhang, W.; Dang, G.; Dong, J.; Li, Y.; Jiao, P.; Yang, M.; Zou, X.; Cao, Y.; Ji, H.; Dong, L. A multifunctional nanoplatform based on graphitic carbon nitride quantum dots for imaging-guided and tumor-targeted chemo-photodynamic combination therapy. *Colloids Surf. B Biointerfaces* **2021**, *199*, 111549. [CrossRef]
46. Chen, Q.; Sun, S.; Lin, H.; Li, Z.; Wu, A.; Liu, X.; Wu, F.-G.; Zhang, W. Supra-Carbon Dots Formed by Fe^{3+}-Driven Assembly for Enhanced Tumor-Specific Photo-Mediated and Chemodynamic Synergistic Therapy. *ACS Appl. Bio Mater.* **2021**, *4*, 2759–2768. [CrossRef]

Disclaimer/Publisher's Note: The statements, opinions and data contained in all publications are solely those of the individual author(s) and contributor(s) and not of MDPI and/or the editor(s). MDPI and/or the editor(s) disclaim responsibility for any injury to people or property resulting from any ideas, methods, instructions or products referred to in the content.